npj | Flexible Electronics

www.nature.com/npjflexelectron

ARTICLE OPEN

Check for updates

# Short-wave infrared organic phototransistors with strong infrared-absorbing polytriarylamine by electron-transfer doping

Chulyeon Lee[1], Hwajeong Kim[1,2] and Youngkyoo Kim[1]✉

Short-wavelength infrared (SWIR) sensors have attracted keen attention due to the increasing necessity in a variety of scientific and industrial applications, including biomedical and information technology fields. Because conventional SWIR sensors are made of inorganic materials with rigid and brittle characteristics, organic materials with a discrete SWIR absorption are required for flexible SWIR sensors in the flexible electronics era. Here, we demonstrate that a polytriarylamine, poly[N,N′-bis(4-butylphenyl)-N,N′-bis (phenyl)benzidine] (PolyTPD), can absorb almost full range of SWIR wavelength ($\lambda = 1000–3200$ nm) after 48 h doping with tris (pentafluorophenyl)borane (BCF). The spectroscopic characterization disclosed that an electron transfer from PolyTPD to BCF created a new low energy level (gap) state leading to the SWIR absorption in the BCF-doped PolyTPD complexes. Organic phototransistors (OPTRs) with the BCF-doped PolyTPD films as a gate-sensing layer could detect the SWIR light with a reasonable photoresponsivity of ~538 mA $W^{-1}$ ($\lambda = 1500$ nm), ~541 mA $W^{-1}$ ($\lambda = 2000$ nm), and ~222 mA $W^{-1}$ ($\lambda = 3000$ nm). The present breakthrough SWIR-OPTR technology can pave a way for further advances in SWIR-absorbing organic materials and flexible SWIR sensors.

*npj Flexible Electronics* (2021)5:10 ; https://doi.org/10.1038/s41528-021-00105-z

## INTRODUCTION

Infrared (IR), which is invisible to human eyes, has been widely used for various applications, such as optical communication, night vision, light detection and ranging, thermal imaging (temperature monitoring), IR spectroscopy, biomedical imaging, etc.[1–10]. According to the wavelength ($\lambda$) of IR, the IR range can be further divided into five categories: near-infrared (NIR, $\lambda = 0.75–1.4$ μm), short-wavelength infrared (SWIR, $\lambda = 1.4–3$ μm), mid-wavelength infrared (MWIR, $\lambda = 3–8$ μm), long-wavelength infrared (LWIR, $\lambda = 8–15$ μm), and far infrared (FIR, $\lambda = 15–1000$ μm)[11]. To date, the detection of IR could be possible using sensors based on inorganic materials, for example, silicon and germanium for NIR, indium gallium arsenide (InGaAs) for NIR and SWIR, indium antimonide (InSb) and mercury cadmium telluride (HgCdTe) for MWIR and LWIR, platinum silicide (PtSi; or microbolometers) for LWIR, etc.[12–15]. In particular, SWIR has become one of the important IR categories because it can detect further things underneath the surface of objects thanks to its capability of penetration deeper than a shorter wavelength light (visible and NIR) and reflection like a visible light (different from MWIR and LWIR that emit heats)[16]. However, the inorganic materials for conventional SWIR sensors have a demerit of rigid (hard) and/or brittle characteristics (and high-temperature processes), which are undesirable for flexible IR detectors[17–19]. Therefore, flexible SWIR-sensing materials are required to replace conventional inorganic materials[20–23].

In this regard, keen attention has been paid to IR-absorbing organic materials because organic thin films can be generally flexible due to the existence of free volumes among molecules[24–27]. In principle, the IR absorption of organic materials can be practically realized by narrowing molecular orbital energy levels (band gaps) by two approaches: (1) covalent bonding approach by combining atoms and/or functional groups with largely different energy levels (i.e., electron-donating and electron-accepting groups), and (2) doping approach by forming new energy levels (gap states) via introduction of chemical and/or physical dopants[28,29]. To date, very limited number of IR-absorbing organic materials have been reported by the covalent bonding approach and their IR absorption range was below $\lambda = 1800$ nm (NIR but very small part of SWIR; see Supplementary Table 1)[30–32]. In contrast, the doping approach delivered extremely shifted IR absorption up to $\lambda = 2000$ nm, which is supported by well-known conducting polymers, such as poly(3,4-ethylenedioxythiophene):poly(styrenesulfonate) (PEDOT:PSS) and polyaniline:camphorsulfonic acid (PANI:CSA)[33,34]. The PEDOT:PSS and PANI:CSA polymers have been reported to exhibit a broad range of IR absorption from $\lambda =$ ca. 1000 nm to $\lambda =$ ca. 2000 nm[35,36]. However, these doped polymers could not attract much attention as an IR sensor because of their predominant applications for electrodes and/or interfacial charge transport layers thanks to the versatile electrical conductivity[37–40]. Recently, it has been reported that the optical absorption range of poly(3-hexylthiophene) (P3HT) can be extended up to ca. 1100 nm (NIR range) by doping it with tris(pentafluorophenyl)borane (BCF)[41,42].

However, these doped polymers (PEDOT:PSS etc.) showed too broad IR absorptions, which can be a disadvantage for the development of discrete SWIR-sensing detectors (not disturbed by a longer wavelength IR) such as SWIR-sensing organic phototransistors (SWIR-OPTRs) with a signal amplification and active matrix driving capability[43]. The reason why such too broad IR absorptions were made for the conventional doped polymers can be ascribed to the long conjugation lengths along with the conjugated polymer chains[44,45]. Therefore, a controlled

[1]Organic Nanoelectronics Laboratory and KNU Institute for Nanophotonics Applications (KINPA), Department of Chemical Engineering, School of Applied Chemical Engineering, Kyungpook National University, Daegu, Republic of Korea. [2]Priority Research Center, Research Institute of Environmental Science & Technology, Kyungpook National University, Daegu, Republic of Korea. ✉email: ykimm@knu.ac.kr

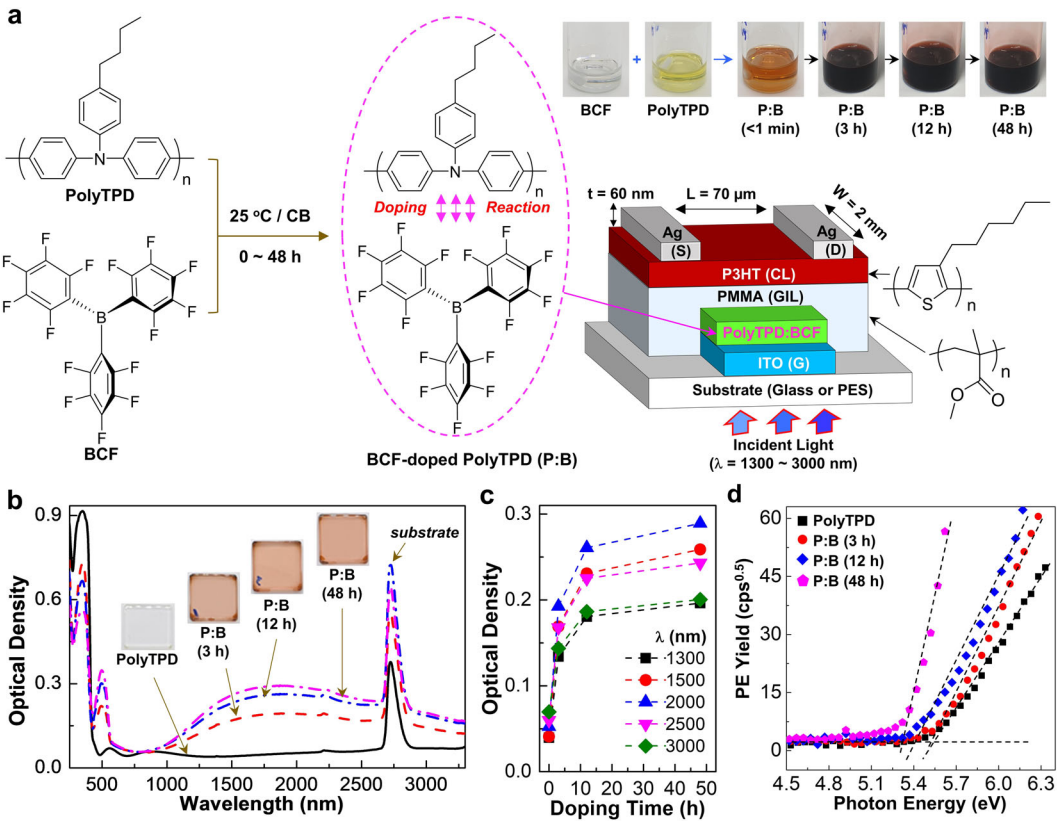


**Fig. 1 Doping reaction for SWIR absorption and device structure. a** Scheme for the doping reaction between PolyTPD and BCF (see photographs of solutions according to the doping time on the right top) and illustration of the SWIR-OPTR structure with the BCF-doped PolyTPD GSL (right bottom). **b** Optical absorption spectra of the BCF-doped PolyTPD (PolyTPD:BCF = P:B) films coated on quartz substrates (annealed at 120 °C for 30 min) according to the doping time (inset: corresponding photographs). **c** Optical density as a function of doping time at various wavelengths (data taken form **b**). **d** Photoelectron (PE) yield spectra for the BCF-doped PolyTPD films annealed at 120 °C for 30 min.

conjugation length is considered to deliver a managed absorption range suitable for SWIR by varying the parameters, such as backbone structure of conjugated polymers, types of dopants, doping time and temperature, dopant concentration, etc.

In this study, we demonstrate that the well-controlled SWIR absorption (up to $\lambda = \sim 3200$ nm) can be achieved from a polytriarylamine, poly[N,N′-bis(4-butylphenyl)-N,N′-bis(phenyl) benzidine] (PolyTPD), by the time-dependent BCF doping at a fixed BCF concentration. The SWIR absorption intensity of the BCF-doped PolyTPD films was gradually increased with the doping time at a fixed BCF concentration of PolyTPD:BCF (P:B = 1:1 by weight or molar ratio) and almost saturated at 48 h. The optimized BCF-doped PolyTPD films were applied as a gate-sensing layer (GSL) in a geometry of organic field-effect transistors (OFETs). The device results showed that the SWIR-OPTRs with the BCF-doped PolyTPD GSLs could successfully detect the SWIR light up to $\lambda = 3200$ nm with high sensing stability and the SWIR sensitivity could be controlled by adjusting the gate voltage.

## RESULTS

### Doping reaction leading to strong SWIR absorption

The doping reaction between PolyTPD and BCF was first examined by adding the BCF solution (40 mg ml$^{-1}$, chlorobenzene (CB)) to the PolyTPD solution (40 mg ml$^{-1}$, CB) at room temperature (25 °C). As seen from the chemical structures in Fig. 1a, neither PolyTPD nor BCF has a reactive functional group so that no chemical reactions involving the formation of covalent bonds and/or ionic moieties can be expected from the present mixed solutions. Upon adding the BCF solution to the PolyTPD solution, the solution color was noticeably changed and darkened with time (see Fig. 1a right top and Supplementary Fig. 1). Considering the change of solution colors with time, the doping reaction might be very quick and enter a stabilizing stage after 3 h at room temperature. In addition, no clues on any reverse reaction (de-doping) could be observed from the solutions reacted up to 48 h.

To further understand, the optical absorption spectra were measured for the PolyTPD:BCF (P:B) films that were coated from corresponding solutions with different doping time. As shown in Fig. 1b, the PolyTPD:BCF film from the mixture solution reacted for 3 h delivered a new broad optical absorption peak at a wavelength ($\lambda$) range between 1000 and >3200 nm. This new absorption peak was quickly grown up to 10 h and then its intensity was slowly increased (see Fig. 1c and Supplementary Fig. 2). Similarly, a new optical absorption peak was also found in the visible range between $\lambda = 420$ nm and $\lambda = 570$ nm, and grown with the doping time (refer to the optical absorption spectrum of BCF in Supplementary Fig. 3). A close look into the optical absorption peaks in the UV–visible range finds that the original absorption peak (between $\lambda = 280$ nm and $\lambda = 420$ nm) of PolyTPD was gradually decreased with the doping time (see Supplementary Fig. 4). This phenomenon means that the density of state (ground) in PolyTPD was decreased by the doping reaction leading to the formation of two states: (1) $\lambda = 420$–$570$ nm and (2) $\lambda = 1000$–$3200$ nm (and higher).

As a consequence, the ionization potential was gradually reduced for the PolyTPD:BCF (BCF-doped PolyTPD) films with the doping time ($t_D$) (Fig. 1d and Supplementary Fig. 5), indicative of the lowering in the highest occupied molecular orbital (HOMO)

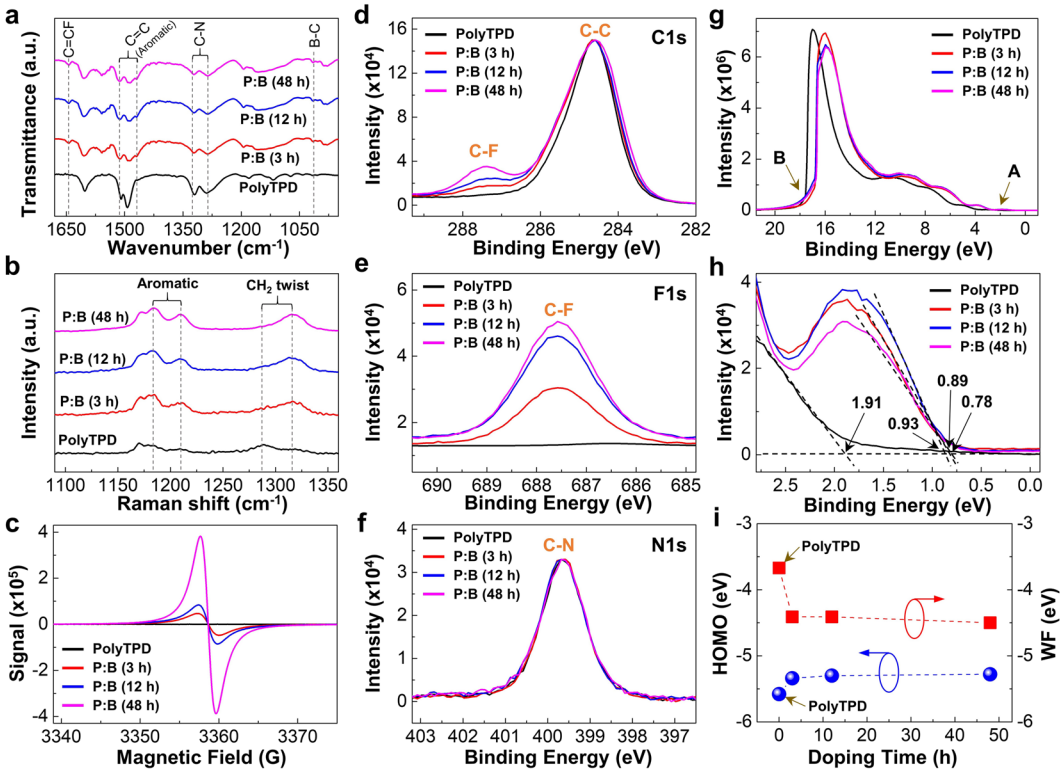


**Fig. 2 Spectroscopic analysis according to doping time. a** FT-IR spectra, **b** Raman spectra, **c** ESR spectra, **d**–**f** XPS spectra (C1s, F1s, and N1s), **g**, **h** UPS spectra, and **i** change of the HOMO energy level and work function (WF) for the BCF-doped PolyTPD (P:B) films annealed at 120 °C for 30 min.

energy of PolyTPD by the BCF doping. The resulting PolyTPD:BCF films were employed as a GSL for the SWIR-sensing OPTRs, as illustrated in Fig. 1a (right bottom)[24]. It is worthy to note that the PolyTPD:BCF layers were well formed and stable without any deformation upon wet coatings of subsequent polymeric layers because they were insoluble in *n*-butyl acetate (NBA) solvent used for the poly(methyl methacrylate) (PMMA) layer (see Supplementary Fig. 6).

## Spectroscopic characterizations and doping mechanism

The atomic and molecular level changes in PolyTPD by the BCF doping was investigated by various spectroscopic measurements on the PolyTPD:BCF films. The Fourier transform-infrared (FT-IR) spectra confirm the existence of BCF in the PolyTPD:BCF films because C = C–F (1645 $cm^{-1}$) and B–C (1015 $cm^{-1}$) peaks were measured together with a broadened C = C shoulder at ~1510 $cm^{-1}$ (see Fig. 2a and Supplementary Fig. 7). The peak intensity of C–N stretching at 1320 $cm^{-1}$ was gradually reduced with the doping time, which can be attributable to the change of nitrogen environment by the BCF doping[46,47]. The existence of BCF can be further evidenced by the doping time-dependent Raman intensity change for the aromatic peaks at ~1185–1210 $cm^{-1}$ (see Fig. 2b and Supplementary Fig. 8). The intensity ratio of the $CH_2$ twist peaks at 1290–1315 $cm^{-1}$ was considerably changed by the BCF doping, which can be ascribed to a large-scale rearrangement of butyl groups in PolyTPD by the binding (doping) of BCF molecules to the PolyTPD chains.

As shown in Fig. 2c, an electron spin resonance (ESR) signal was measured at ~3355 G for the PolyTPD:BCF films even though no ESR signal was detected for the pristine PolyTPD film. This result indicates the generation of unpaired (single) electrons in the PolyTPD:BCF films. Further investigation finds that the ESR signal became intensified as the doping time increased, which can be directly related to the increased number of unpaired electrons with the doping time. In other words, the ESR results confirm that the doping reaction between PolyTPD and BCF is dependent on the doping time. Next, the core level environment of atoms in the PolyTPD:BCF films was investigated with X-ray photoelectron spectroscopy (XPS). The intensity of C1s and F1s peaks (in BCF) was gradually increased with the doping time, but the binding energy (BE) of these XPS peaks was almost unchanged (Fig. 2d, e). The same trend was measured for the N1s peak (in PolyTPD), as can be clearly observed in Fig. 2f. This result reflects that the extent of doping reaction between PolyTPD and BCF was increased with time, but the core level environment of atoms was not affected by the doping reaction.

For further understanding, the detailed energy level (band) change in PolyTPD by the BCF doping was investigated with ultraviolet photoelectron spectroscopy (UPS). As shown in the UPS spectra (Fig. 2g), a pronounced spectral shift toward a lower BE direction was measured for the PolyTPD:BCF films compared to the pristine PolyTPD film. A close look into the valence band (level) edge region (A in Fig. 2g) finds that the onset BE of PolyTPD was largely shifted from 1.91 to ca. 0.78 eV by the BCF doping (see Fig. 2h). This means that the extraction of electrons became relatively easier for the PolyTPD:BCF films than the pristine PolyTPD film, which is in agreement with the ionization potential change in Fig. 1d. As shown in Fig. 2h, the calculated HOMO energy level was abruptly shifted from −5.58 eV (pristine PolyTPD film) to −5.34 eV by the BCF doping for 3 h, and then further to −5.28 eV after 48 h (see Supplementary Fig. 9 for the detailed calculations). Note that the HOMO energy level of the pristine PolyTPD molecules dissolved in dichloromethane (solvent) was measured to −5.48 eV with cyclic voltammetry (CV; see Supplementary Fig. 10a).

Based on the above characterization results, it is proposed that the doping reaction between PolyTPD and BCF occurs via the electron transfer from PolyTPD to BCF on a molecular scale, as

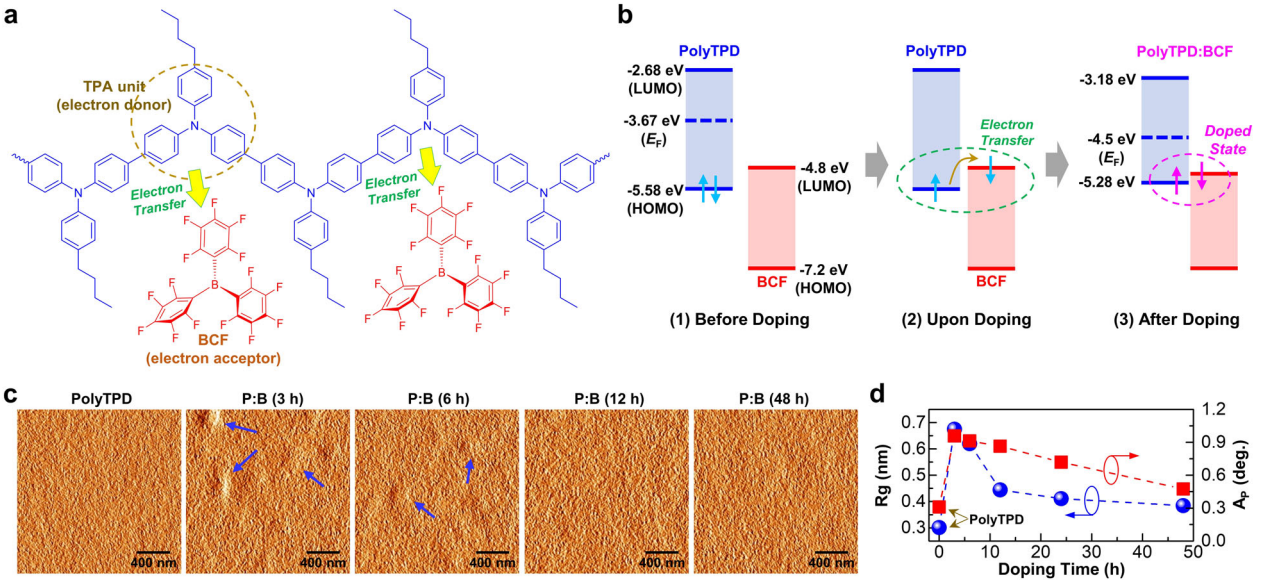


**Fig. 3 Change of energy level and morphology. a** Illustration for the electron transfer between PolyTPD and BCF. **b** Flat energy level (band) diagrams for the explanation of electron transfer-mediated doping mechanism between PolyTPD and BCF. **c** Phase-mode AFM images (2 μm × 2 μm) for the PolyTPD:BCF films (48 h) according to the doping time. **d** Change of root-mean-square roughness (*Rg*) and phase angle ($A_P$) according to the doping time for the PolyTPD:BCF films (48 h).

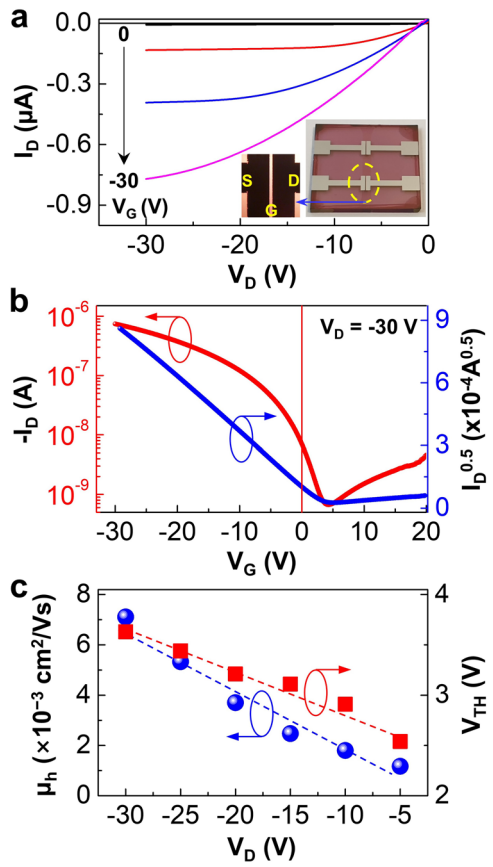


**Fig. 4 Basic OFET characteristics. a** Output and **b** transfer curves for the OFETs with the PolyTPD:BCF layers (48 h; inset: photographs for the devices) in the dark. **c** Change of hole mobility ($\mu_h$) and threshold voltage ($V_{TH}$) as a function of drain voltage (data were taken from the transfer curves in Supplementary Fig. 12).

illustrated in Fig. 3a. In more detail, the TPA units of PolyTPD act as an electron donor, while the BCF molecules play as an electron-accepting role in the doping reaction. This electron transfer-based doping reaction can be further explained by the three-step process leading to the change of energy level (band), as depicted in Fig. 3b. The electron transfer upon doping reaction in solutions leads to a positive polaron state (radical cation) in PolyTPD, while it bestows a negative state (radical anion) to BCF (see the middle diagram in Fig. 3b). In terms of PolyTPD, the HOMO energy level was increased from −5.58 eV (pristine PolyTPD film) to −5.28 eV (PolyTPD:BCF film), but the LUMO energy level was decreased from −2.68 eV (pristine PolyTPD film) to −3.18 eV (PolyTPD:BCF film) by the BCF doping (all data were taken from the UPS spectra of film samples). Note that the HOMO and LUMO energy levels of BCF molecules (in solution) in Fig. 3b were taken from previous reports (our CV measurement could deliver only the LUMO energy level of −5.01 eV for the BCF solution as given in Supplementary Fig. 10b)[48]. Here, a coulombic interaction between these counter charges may occur, leading to physically binding the two charged species in the films, so that the BCF-doped PolyTPD components can be kept in the films without removal upon spin-coating processes. Therefore, the BCF-doped PolyTPD complexes have new energy (gap) states with the lowest energy of ca. −5.28 eV that can be corresponded to the optical absorption edge ($\lambda$ = ca. 3200 nm; see Fig. 1b). Considering a possible interaction of BCF molecules to various conformational states of the PolyTPD chains, the BCF-doped PolyTPD complexes are regarded to make a broad range of energy states as measured from the absorption spectra ($\lambda$ = 420–570 nm and $\lambda$ = 1000–3200 nm in Fig. 1b). Note that the new optical absorption peaks ($\lambda$ = 420–570 nm) can be assigned to the optical transition between the HOMO (−5.28 eV) and LUMO (−3.18 eV) energy levels of the BCF-doped PolyTPD complexes, when it comes to the band edge of these peaks (ca. 590 nm, 2.1 eV). Finally, the atomic force microscope (AFM) images unveiled an uneven morphology featuring a nanodot in the PolyTPD:BCF films, which are varied with the doping time (Fig. 3c and Supplementary Fig. 11). The nanodots were relatively more pronounced at 3 h and became gradually degenerated with the doping time, as supported by the root-mean-square roughness (*Rg*) and phase angle changes in Fig. 3d. It is speculated that the

nanodots might be formed due to the existence of heterogeneous states that are related to the pristine PolyTPD and BCF-doped PolyTPD phases.

### Transistor performances in the dark

The OFETs with the BCF-doped PolyTPD layers (48 h) placed between the indium-tin oxide (ITO) electrodes and the PMMA layers were examined in the dark. As shown in Fig. 4a, the output curves deliver a typical behavior of p-channel transistors when it comes to the drain current ($I_D$) change according to the drain voltage ($V_D$) at a fixed gate voltage ($V_G$). In addition, the drain current in the output curves became saturated as the drain voltage increased, indicative of proper working of field-effect transistors. The transfer curves in Fig. 4b clearly exhibited the characteristics of p-channel transistors as the drain current was pronouncedly increased with the gate voltage. It is noted that a good linearity was obtained for the $I_D^{0.5}$–$V_G$ plot, implying a constancy in charge transport with the gate voltage in spite of the presence of the PolyTPD:BCF layers. As shown in Fig. 4c, the hole mobility ($\mu_h$) and threshold voltage ($V_{TH}$) were almost linearly changed with the drain voltage (see all transfer curves in Supplementary Fig. 12). This result supports the voltage-dependent stable characteristics of the present OFETs with the BCF-doped PolyTPD layers (48 h).

### SWIR light-sensing device characteristics

The SWIR light-sensing performance was tested by illuminating three different monochromatic SWIR light ($\lambda = 1500$, 2000, and 3000 nm) to the channel area of the OFETs with the PolyTPD:BCF layers (48 h). The incident light intensity ($P_{IN}$) was adjusted to 72, 58, and 42 μW cm$^{-2}$ at $\lambda = 1500$, 2000, and 3000 nm, respectively. As observed from the output curves in Fig. 5a–c, the drain current was certainly increased upon illumination with the SWIR light irrespective of the gate voltage. The higher the gate voltage, the higher the drain current in the output curves for all the three SWIR cases. This result basically indicates that the PolyTPD:BCF layers (48 h) work properly as a GSL for the SWIR light up to $\lambda = 3000$ nm, achieving a SWIR-OPTR. As shown in Fig. 5d–f, the drain current in the transfer curves was noticeably increased by the SWIR illumination over the whole gate voltage. A particular attention is paid to the SWIR-driven huge jump in drain current at around turn-on voltage region, which could lead to the shift of threshold voltage toward a lower gate voltage direction (in an absolute value). Note that almost no meaningful change of drain current and threshold voltage was measured for the OFETs with the pristine PolyTPD layer (in the GSL position) under illumination with the three different SWIR light (see Supplementary Fig. 13).

To investigate the detailed performances of the present SWIR-OPTRs, the photoresponsivity ($R_C$), representing the ratio of net photocurrent to incident light intensity after removing the dark drain current, was extracted from the transfer curves (see Fig. 5g–i). As the gate voltage increased (negatively), the photoresponsivity was initially increased and levelled off at the highest drain voltage ($V_D = -30$ V). However, irrespective of the SWIR wavelength, the photoresponsivity was decreased again after reaching a maximum at the lower drain voltages. The initial rise in $R_C$ can be assigned to the increased collection efficiency of photogenerated charges with the gate voltage, whereas the saturating and/or decreasing $R_C$ afterward can be attributed to the narrowing of neutral zones for photoexcitation in the GSLs, owing to the overwhelming of field-effect zones[49,50]. Because this phenomenon was similarly measured for the three different SWIR, the present SWIR-OPTRs with the PolyTPD:BCF GSLs are considered to work with the same mechanism of photoexcitation and charge generation/separation in spite of a large energy gap in the incident SWIR light (0.83 eV at $\lambda = 1500$ nm, 0.62 eV at $\lambda = 2000$ nm, and 0.41 eV at $\lambda = 3000$ nm). The ratio ($R_C/R_T$) of $R_C$ to theoretical maximum photosensitivity ($R_T$), which is irrelevant to the kind of materials, reached 45% ($\lambda = 1500$ nm), 41% ($\lambda = 2000$ nm), and 16% ($\lambda = 3000$ nm) at $V_G = V_D = -30$ V, respectively (see inset graphs in Fig. 5g–i).

### Sensing mechanism and flexible SWIR-OPTRs

On the basis of above results, a possible three-step mechanism can be proposed for the operation of the present SWIR-OPTRs with the PolyTPD:BCF GSLs (see Fig. 6a): (1) the field-effect charges are generated in each layer by applying the negative drain and gate voltages to the corresponding electrodes. The field-effect charges lead to the deformation in the energy levels (bands) inside devices (see Supplementary Fig. 14). This first step enables the SWIR-OPTRs to turn on and ready for operation. (2) When the SWIR light is illuminated to the channel area, it passes through the P3HT and PMMA layers without absorption and reaches the PolyTPD:BCF GSLs. Then the PolyTPD:BCF GSLs absorb the SWIR light leading to the generation of excitons, which is instant and may not largely change the energy levels when it comes to the neutral state of excitons. (3) The excitons generated in the PolyTPD:BCF GSLs are subjected to a field-induced charge separation process leading to the rearrangement of individual charges (holes and electrons). These individual charges act as an additional electric field inside the devices so that more holes can be formed in the P3HT channel layers (see the deformed energy levels due to the photogenerated charge build-up). The resulting photocurrent ($I_{SWIR}$) is added to the original field-effect current ($I_{FET}$), which leads to the increased drain current in the devices upon the SWIR illumination.

For a possible application of the present SWIR-OPTR technology to flexible electronics, the flexible SWIR-OPTRs with the PolyTPD:BCF GSLs were fabricated using the ITO-coated poly(ethylene naphthalene) (PEN) film substrates. As shown in Fig. 6b, the drain current in the transfer curves was noticeably increased upon illumination with the SWIR light ($\lambda = 1500$, 2000, and 3000 nm; see the dark characteristics in Supplementary Fig. 15). It is worthy to note that the threshold voltage in the transfer curves was pronouncedly shifted by the SWIR illumination, which is in accordance with the phenomena in the case of using the glass substrates (see Fig. 5). As shown in Fig. 6c, the present flexible SWIR-OPTRs exhibited a good sensing stability upon on/off modulations of the incident SWIR light ($P_{IN} = 58$ μW cm$^{-2}$ at $\lambda = 2000$ nm and 42 μW cm$^{-2}$ at $\lambda = 3000$ nm). In order to examine the durability of the flexible SWIR-OPTRs, the device performances in the dark were measured before and after bending at a radius of curvature of 7.5 mm. The result showed that the output and transfer curves were almost similar (very small change) even after bending (see Supplementary Fig. 16). In particular, the bended flexible SWIR-OPTRs (bended state at a radius of curvature of 7.5 mm) exhibited noticeable drain current increase and threshold voltage shift upon illumination with the three different SWIR light (see Supplementary Fig. 17). In addition, the drain current from the bended flexible SWIR-OPTRs was gradually increased with the applied gate and/or drain voltages. This result reflects that the PolyTPD:BCF layers play a durable GSL in the sensing of SWIR light even in the geometry of flexible substrates.

## DISCUSSION

The present breakthrough work showed that a triarylamine-based polymer (PolyTPD) could be successfully doped with a fluorinated small molecule with high electron affinity (BCF), and the resulting doped polymer (BCF-doped PolyTPD) films were able to act as an efficient GSL for SWIR-OPTRs. The BCF-doped PolyTPD was found to have a newly evolved optical absorption peak, covering a broad

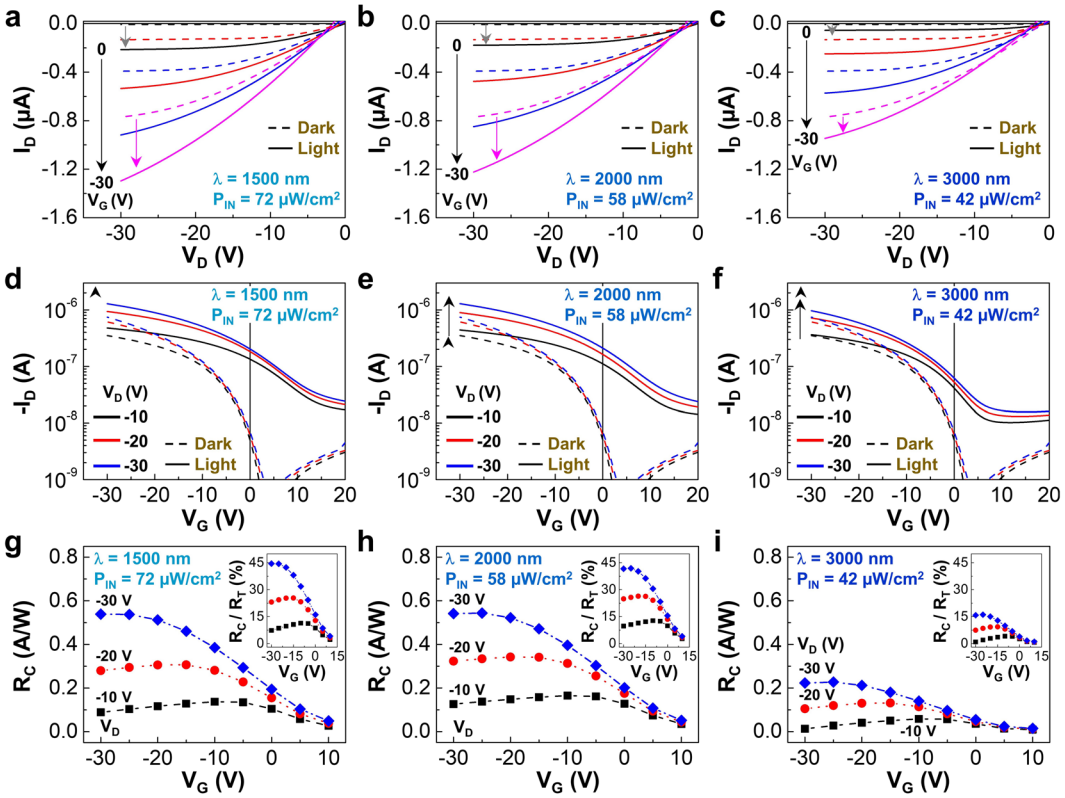


**Fig. 5 Device characteristics under SWIR illumination. a–c** Output and **d–f** transfer curves for the SWIR-OPTRs with the PolyTPD:BCF GSLs (48 h) upon illumination with three different SWIR light ($\lambda = 1500$, 2000, and 3000 nm). Note that $V_G$ and $V_D$ were negatively increased by −10 V in the output and transfer curves, respectively. **g–i** Photoresponsivity ($R_C$) as a function of $V_G$ at three different drain voltages under illumination with the SWIR light ($\lambda = 1500$, 2000, and 3000 nm; inset: the ratio of the measured photoresponsivity to the theoretical maximum photoresponsivity ($R_T$) at a given wavelength). Note that all $R_C$ values were obtained after removing the dark current from the transfer curves in **d**, **e**, and **f**.

range of NIR and SWIR between 1000 and >3200 nm, which was gradually increased upon doping reaction up to 48 h at room temperature. The in-depth spectroscopic analysis unveiled that the doping reaction between PolyTPD and BCF occurs by the ground-state electron transfer from PolyTPD to BCF on a molecular scale. The single (unpaired) electrons remained in PolyTPD after doping were clearly measured by the ESR measurement, while the HOMO energy level shift in the BCF-doped PolyTPD film was confirmed by the photoelectron spectroscopy measurements. The AFM examination revealed the presence of heterogeneous states during doping, which might be originated by the co-existence of two different phases (the pristine PolyTPD and BCF-doped PolyTPD domains). The OFETs with the BCF-doped PolyTPD layers delivered typical p-channel transistor characteristics in the dark. Upon illumination with the SWIR light (1500, 2000, and 3000 nm), the BCF-doped PolyTPD layers could act as an efficient SWIR-detecting GSL in the SWIR-OPTRs. The $R_C$ of the SWIR-OPTRs with the BCF-doped PolyTPD GSLs reached ~538 mA $W^{-1}$ ($\lambda = 1500$ nm), ~541 mA $W^{-1}$ ($\lambda = 2000$ nm), and ~222 mA $W^{-1}$ ($\lambda = 3000$ nm), which correspond to 45, 41, and 16% of the theoretical responsivity at each wavelength. Further improvement in photoresponsivity can be achievable by optimizing the thickness of BCF-doped PolyTPD layers, doping concentrations, multilayer structures, etc. Finally, the flexible SWIR-OPTRs showed stable sensing characteristics upon on/off modulations of the incident SWIR light. Hence, the present pioneering work is expected to be a stepping stone toward a wide-spreading of the ground-state doping research of nitrogen-containing polymers and their applications for efficient SWIR-sensing photodetectors required for next-generation soft/flexible electronics.

## METHODS

### Materials and solutions

PolyTPD (average molecular weight = 24 kDa) and BCF (formula weight = 511.98) were purchased from Lumtec (Hsin-Chu, Taiwan) and Sigma Aldrich Co. (St Louis, Mo, USA), respectively. P3HT (weight-average molecular weight = 70 kDa, polydispersity index = 1.7, regioregularity >97%) and PMMA (weight-average molecular weight = 120 kDa, polydispersity index = 2.2) were received from Rieke Metals (Lincoln, NE, USA) and Sigma Aldrich (St Louis, Mo, USA), respectively. The P3HT solutions were prepared using toluene (Sigma Aldrich) at a solid concentration of 12.5 mg $ml^{-1}$, while NBA (Sigma Aldrich) was used as a solvent for the preparation of the PMMA solutions (concentration = 80 mg $ml^{-1}$). All solutions were continuously stirred at 60 °C for 24 h before spin-coating.

### Doping reaction and film preparation

To dope PolyTPD with BCF, the binary solutions of PolyTPD (P) and BCF (B) (P:B = 1:1 by weight) were prepared at a solid concentration of 40 mg $ml^{-1}$ using CB as a solvent. These solutions were subjected to continuous stirring on a hot plate stirrer at a fixed temperature of 25 °C by varying the doping time up to 168 h. These solutions were carefully monitored and one solution per every 1 h was taken for spin-coating, in order to examine the change in color and optical absorption spectrum. The BCF-doped PolyTPD films (thickness = 60 nm) were spin-coated on quartz substrates and thermally treated at 120 °C for 30 min for the optical measurements. For the spectroscopic and morphological measurements (FT-IR, XPS, PEYS, UPS, AFM, and scanning electron microscope (SEM)), the same spin-coating processes were applied to prepare the BCF-doped PolyTPD films on the ITO-coated glass substrates, in order to secure the same condition as for the device fabrication. However, for the ESR spectroscopy measurement, the BCF-doped PolyTPD films were prepared on a PEN substrate (width: 3 mm, length: 20 mm) in order to get unperturbed electron spin signals.

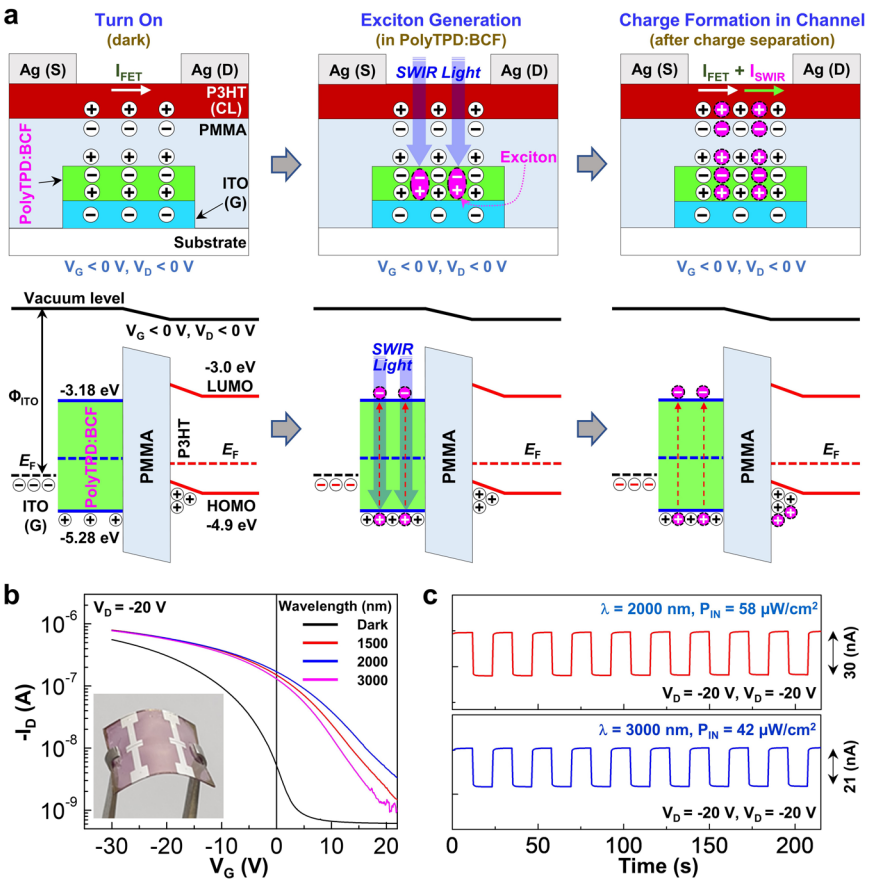


**Fig. 6 Working mechanism and flexible SWIR-OPTRs. a** Proposed mechanism for the operation of the SWIR-OPTRs with the PolyTPD:BCF GSLs under the SWIR illumination (top: device structures, bottom: energy level diagrams): (left) turned-on state in the dark; (middle) exciton generation in the PolyTPD:BCF GSLs upon illumination with the SWIR light; (right) charge separation from photogenerated excitons and formation of induced charges in the channel layer. $\Phi_{ITO}$, $I_{FET}$, $I_{SWIR}$, and $E_F$ stand for the work function of ITO gate electrode, the drain current by field-effect phenomenon, the drain current by SWIR illumination, and Fermi energy level, respectively. **b** Transfer curves ($V_D = -20$ V) for the flexible SWIR-OPTRs with the PolyTPD:BCF GSLs (48 h) under illumination with the SWIR light ($\lambda = 1500$, 2000, and 3000 nm). **c** Change of photocurrent upon optical modulations of the incident SWIR light ($\lambda = 2000$ and 3000 nm) for the flexible SWIR-OPTRs.

## Device fabrication

To fabricate SWIR-OPTRs, the ITO-coated glass substrates (sheet resistance $= 10\ \Omega\ cm^{-2}$) were underwent via a photolithography process for the patterning of the ITO stripe (1 mm × 12 mm) used as a gate (G) electrode. The patterned ITO–glass substrates were subjected to wet-clean processes using acetone and isopropyl alcohol (30 min), followed by dry cleaning steps using a UV-ozone cleaner (28 mW $cm^{-2}$ for 20 min, Ahtech, Korea). The BCF-doped PolyTPD layers (thickness = 60 nm) were deposited on the patterned ITO–glass substrates by spin-coating at 2000 r.p.m. for 60 s. The side parts of the coated BCF-doped PolyTPD layers were removed using CB to achieve the final BCF-doped PolyTPD stripes (1.1 mm × 12 mm), followed by thermal treatment at 120 °C for 30 min. Next, the PMMA gate-insulating layers (thickness = 450 nm) were spin-coated on the patterned BCF-doped PolyTPD layers at 2000 r.p.m. for 60 s and thermally treated at 120 °C for 30 min. Finally, the P3HT channel layers (thickness = 60 nm) were spin-coated on the PMMA layers at 1500 r.p.m. for 30 s and soft-baked at 70 °C for 15 min. These polymer multilayer samples were transferred to a vacuum chamber installed inside a nitrogen-filled glovebox system. When the base pressure reached ca. $1 \times 10^{-6}$ torr, silver (Ag) metals were thermally evaporated on the P3HT layers through a shadow mask to make the 60-nm-thick source (S) and drain (D) electrodes. The channel length and width of the SWIR-OPTRs were 70 μm and 2 mm, respectively. All devices and film samples were wrapped and safely stored inside the argon-filled glovebox until measurements.

## Measurement and characterizations

The thickness of films was measured using a nanoscale surface profiler (DektakXT, Bruker, USA). The optical absorption spectra of solutions and films were measured using a UV/Vis/NIR spectrometer (Lambda 750, PerkinElmer, Houston, TX, USA). A FT-IR spectrometer (5700 Continum, Thermo Scientific, Inc.) was used to characterize specific functional groups in the film samples in an attenuated total reflection mode. The Raman spectra of films were measured using a Raman spectrometer (Almega X, Thermo Scientific, Inc.) at an excitation wavelength of 532 nm. The core level atom enivronments in the films were characterized by employing an XPS spectrometer (ESCALAB 250, Thermo Scientific, Inc.). The HOMO energy level change of the BCF-doped PolyTPD films were measured and characterized using a UPS spectrometer (Nexsa-XPS system, Thermo Scientific, Inc.). The ionization potentials of films were measured using a PE yield spectrometer (PEYS, AC-2, Rieken-Keikki, Japan). The CV measurements were performed for the pristine solutions of PolyTPD and BCF (solvent: dichloromethane) using an electrochemical measurement system equipped with a potentiostat/impedance analyzer (Versastat 4, Ametek, Inc.; see further details in Fig. S10). The existence of radicals (unpaired electrons) in films was investigated by employing an ESR spectrometer (EMXplus-9.5/2.7, Bruker, USA). The surface morphology of film samples was measured using an AFM (Nanoscope IVa, Digital Instruments, Tonawanda, NY, USA), while the film surface and cross-section parts of SWIR-OPTRs were measured using a high-resolution SEM (SU-8230, Hitachi, Japan). The characteristics (output and transfer curves) of OFET devices were measured using a semiconductor parameter analyzer (4200 SCS, 2636B, Keithley, USA). In order to test the performances of SWIR-OPTRs, the channel area of transistors was illuminated with a monochromatic SWIR light from a monochromator (DK240, Spectral Products, Albuquerque, NM, USA) that spectrally filters the source IR beam generated from an IR emitter system (11 W, ASB-IR-12K, Spectral Products). The incident light intensity ($P_{IN}$) of each monochromatic SWIR light was controlled by employing neutral density filter sets, while the

SWIR light power was exactly measured using an optical power meter (PM100D, Thorlabs, Newton, NJ, USA). Two different approaches for the calculation of device current density ($J_D$) were applied: (1) $J_{D,IP} = I_D/(L \times W)$ in a viewpoint of in-plane (IP) direction (actual current flow direction); (2) $J_{D,OOP} = I_D/(T \times W)$ in a viewpoint of out-of-plane (OOP) direction (SWIR light illumination direction), where $T$, $W$, and $L$ stand for the channel thickness, width, and length, respectively. The $P_{IN}$ value (power density) of SWIR light was calculated with $P_{IN} = P/(L \times W)$, where $P$ is the incident light power (in a unit of $W$). The $R_C$ values from $J_{D,IP}$ were used in Fig. 5 (note that the same trend in $R_C$ was obtained for $J_{D,OOP}$).

Methods and any associated references are available in the online version of the paper.

## DATA AVAILABILITY

The data that support the findings of this study are available from the corresponding author upon reasonable request.

Received: 4 November 2020; Accepted: 16 February 2021;
Published online: 12 April 2021

## REFERENCES

1. Mueller, T., Xia, F. & Avouris, P. Graphene photodetectors for high-speed optical communications. *Nat. Photonics* **4**, 297–301 (2010).
2. Luke, T. D. W. et al. Metabolic profiling of early-lactation dairy cows using milk mid-infrared spectra. *J. Dairy Sci.* **102**, 1747–1760 (2019).
3. Simone, G. et al. Near-infrared tandem organic photodiodes for future application in artificial retinal implants. *Adv. Mater.* **30**, 1804678 (2018).
4. Villaseñor-Aguilar, M. J. et al. A maturity estimation of bell pepper (capsicum annuum l.) by artificial vision system for quality control. *Appl. Sci.* **10**, 5097 (2020).
5. Yang, M. et al. Ultrahigh stability 3D Ti $Bi_2Se_3/MoO_3$ thin film heterojunction infrared photodetector at optical communication waveband. *Adv. Funct. Mater.* **30**, 1909659 (2020).
6. Thomas, L., Sorathiya, V., Patel, S. K. & Guo, T. Graphene-based tunable near-infrared absorber. *Micro. Opt. Technol. Lett.* **61**, 1161–1165 (2019).
7. Saritha Devi, H. N. V., Swapna, M. N. S. & Sankararaman, S. I. Cost-effective green synthesis of boron-rich carbide coatings for infrared windows and night-vision optics. *Phys. Status Solidi A* **217**, 1901014 (2020).
8. Wu, Z., Yao, W., London, A. E., Azoulay, J. D. & Ng, T. N. Elucidating the detectivity limits in shortwave infrared organic photodiodes. *Adv. Funct. Mater.* **28**, 1800391 (2018).
9. Wu, Z. et al. The role of dielectric screening in organic shortwave infrared photodiodes for spectroscopic image sensing. *Adv. Funct. Mater.* **28**, 1805738 (2018).
10. Lin, J. et al. Novel near-infrared II aggregation-induced emission dots for in vivo bioimaging. *Chem. Sci.* **10**, 1219–1226 (2019).
11. Bhowmik, M. K. et al. Thermal infrared face recognition-a biometric identification technique for robust security system. In *Reviews, Refinements and Newldeas in Face Recognition*, Vol. 7 (ed. Corcoran, P. M.) 113–120 (IntechOpen, 2011).
12. Cao, G. et al. Performance of extended wavelength InGaAs/InAsP SWIR detector. In Proc. 7th International Symposium on Advanced Optical Manufacturingand Testing Technologies: Optoelectronics Materials and Devices for Sensing and Imaging. Vol. 9284 (ed. Jiang Y. & Yu, J.) 928406 (SPIE, 2014).
13. Davis, M. & Greiner, M. E. Indium antimonide large-format detector arrays. *Opt. Eng.* **50**, 061016 (2011).
14. Akhavan, N. D., Jolley, G., Umana-Membreno, G. A., Antoszewski, J. & Faraone, L. Design of band engineered HgCdTe nBn detectors for MWIR and LWIR applications. *IEEE Trans. Electron Devices* **62**, 722–728 (2015).
15. Lucey, P. G., Wood, M., Crites, S. T. & Akagi, J. A LWIR hyperspectral imager using a Sagnac interferometer and cooled HgCdTe detector array. In *Proc. Algorithms and Technologies for Multispectral, Hyperspectral, and Ultraspectral Imagery XVIII*. Vol. 8390 (eds Shen, S. S. & Lewis P. E.) 83900 (SPIE, 2012).
16. Hansen, M. P., & Malchow, D. S. Overview of SWIR detectors, cameras, and applications. In Proc. Thermosense XXX. Vol 6939 (eds Vavilov, V. P. & Burleigh, D. D) 69390I (SPIE, 2008).
17. Ouyang, W., Teng, F., He, J. H. & Fang, X. Enhancing the photoelectric performance of photodetectors based on metal oxide semiconductors by charge-carrier engineering. *Adv. Funct. Mater.* **29**, 1807672 (2019).
18. Ni, Z. et al. Plasmonic silicon quantum dots enabled high-sensitivity ultrabroadband photodetection of graphene-based hybrid phototransistors. *ACS Nano* **11**, 9854–9862 (2017).
19. Arquer, F. P. G., Armin, A., Meredith, P. & Sargent, E. H. Solution-processed semiconductors for next-generation photodetectors. *Nat. Rev. Mater.* **2**, 1–17 (2017).
20. Liang, F. X., Wang, J. Z., Li, Z. P. & Luo, L. B. Near-infrared-light photodetectors based on one-dimensional inorganic semiconductor nanostructures. *Adv. Opt. Mater.* **5**, 1700081 (2017).
21. Lou, Z. & Shen, G. Flexible photodetectors based on 1D inorganic nanostructures. *Adv. Sci.* **3**, 1500287 (2016).
22. Teng, F., Hu, K., Ouyang, W. & Fang, X. Photoelectric detectors based on inorganic p-type semiconductor materials. *Adv. Mater.* **30**, 1706262 (2018).
23. Zhao, H. et al. Self-driven visible-near infrared photodetector with vertical CsPbBr3/PbS quantum dots heterojunction structure. *Nanotechnology* **31**, 035202 (2019).
24. Han, H., Lee, C., Kim, H. & Kim, Y. Flexible near-infrared plastic phototransistors with conjugated polymer gate-sensing layers. *Adv. Funct. Mater.* **28**, 1800704 (2018).
25. Lee, C. et al. Organic phototransistors with chemically doped conjugated polymer interlayers for visible and near infrared light detection. *IEEE J. Sel. Top. Quant.* **24**, 1–7 (2018).
26. Kim, H., Wu, Z., Eedugurala, N., Azoulay, J. D. & Ng, T. N. Solution-processed phototransistors combining organic absorber and charge transporting oxide for visible to infrared light detection. *ACS Appl. Mater. Interfaces* **11**, 36880–36885 (2019).
27. Li, N., Lan, Z., Cai, L. & Zhu, F. Advances in solution-processable near-infrared phototransistors. *J. Mater. Chem. C* **7**, 3711–3729 (2019).
28. Suk, J. W. et al. Enhancement of the electrical properties of graphene grown by chemical vapor deposition via controlling the effects of polymer residue. *Nano Lett.* **13**, 1462–1467 (2013).
29. Boonlakhorn, J., Putasaeng, B., Kidkhunthod, P. & Thongbai, P. Improved dielectric properties of (Y+Mg) co-doped $CaCu_3Ti_4O_{12}$ ceramics by controlling geometric and intrinsic properties of grain boundaries. *Mater. Des.* **92**, 494–498 (2016).
30. London, A. E. et al. Donor–acceptor polymers with tunable infrared photoresponse. *Polym. Chem.* **8**, 2922–2930 (2017).
31. Han, J. et al. Low-bandgap donor–acceptor polymers for photodetectors with photoresponsivity from 300 nm to 1600 nm. *J. Mater. Chem. C* **5**, 159–165 (2017).
32. Li, M. et al. Phenanthrene condensed thiadiazoloquinoxaline donor-acceptor polymer for phototransistor applications. *Chem. Mater.* **27**, 2218–2223 (2015).
33. Shi, H. et al. Effective approaches to improve the electrical conductivity of PEDOT: PSS: a review. *Adv. Electron. Mater.* **1**, 1500017 (2015).
34. Cho, S., Lee, J. S. & Joo, H. Recent developments of the solution-processable and highly conductive polyaniline composites for optical and electrochemical applications. *Polymers* **11**, 1965 (2019).
35. Massonnet, N., Carella, A., de Geyer, A., Faure-Vincent, J. & Simonato, J. P. Metallic behaviour of acid doped highly conductive polymers. *Chem. Sci.* **6**, 412–417 (2015).
36. Nizioł, J., Gondek, E. & Plucinski, K. J. Characterization of solution and solid state properties of polyaniline processed from trifluoroacetic acid. *J. Mater. Sci. Mater. Electron.* **23**, 2194–2201 (2012).
37. Enengl, C. et al. Doping-induced absorption bands in p3ht:polarons and bipolarons. *Chemphyschem* **17**, 3836–3844 (2016).
38. Jin, Y., Ye, F., Zeigler, M., Wu, C. & Chiu, D. T. Near-infrared fluorescent dye-doped semiconducting polymer dots. *ACS Nano* **5**, 1468–1475 (2011).
39. An, Q. et al. Improved efficiency of bulk heterojunction polymer solar cells by doping low-bandgap small molecules. *ACS Appl. Mater. Interfaces* **6**, 6537–6544 (2014).
40. Zhao, X., He, S. & Tan, M. C. Design of infrared-emitting rare earth doped nanoparticles and nanostructured composites. *J. Mater. Chem. C* **4**, 8349–8372 (2016).
41. Mansour, A. E. et al. The optical signatures of molecular-doping induced polarons in poly (3-hexylthiophene-2, 5-diyl): individual polymer chains versus aggregates. *J. Mater. Chem. C* **8**, 2870–2879 (2020).
42. Pingel, P. et al. P-type doping of poly (3-hexylthiophene) with the strong lewis acid tris (pentafluorophenyl) borane. *Adv. Electron. Mater.* **2**, 1600204 (2016).
43. Ren, X. et al. Organic field-effect transistor for energy-related applications: low-power-consumption devices, near-infrared phototransistors, and organic thermoelectric devices. *Adv. Energy Mater.* **8**, 1801003 (2018).
44. Randell, N. M., Boutin, P. C. & Kelly, T. L. Bisisoindigo: using a ring-fusion approach to extend the conjugation length of isoindigo. *J. Mater. Chem. A* **4**, 6940–6945 (2016).
45. Jiang, Y. et al. Fused isoindigo ribbons with absorption bands reaching near-infrared. *Angew. Chem.* **130**, 10440–10444 (2018).
46. Ye, T., Wang, J., Chen, W., Yang, Y. & He, D. Improved performance and reproducibility of perovskite solar cells by well-soluble tris(pentafluorophenyl) borane as a p-type dopant. *ACS Appl. Mater. Interfaces* **9**, 17923–17931 (2017).

47. Welch, G. C. & Bazan, G. C. Lewis acid adducts of narrow band gap conjugated polymers. *J. Am. Chem. Soc.* **133**, 4632–4644 (2011).
48. Ye, T., Wang, J., Chen, W., Yang, Y. & He, D. Improved performance and reproducibility of perovskite solar cells by well-soluble tris (pentafluorophenyl) borane as a p-type dopant. *ACS Appl. Mater. Interfaces* **9**, 17923–17931 (2017).
49. Hwang, H. et al. Organic phototransistors with nanoscale phase-separated polymer/polymer bulk heterojunction layers. *Nanoscale* **3**, 2275–2279 (2011).
50. Nam, S. et al. Efficient deep red light-sensing all-polymer phototransistors with p-type/n-type conjugated polymer bulk heterojunction layers. *ACS Appl. Mater. Interfaces* **9**, 14983–14989 (2017).

## ACKNOWLEDGEMENTS

This work was financially supported by the National Research Foundation (NRF) of Korea (NRF_2018R1D1A3B07046214, NRF_2018R1D1A1B07051075, Basic Science Research Program_2018R1A6A1A03024962) and the International Cooperative R&D program funded by the Ministry of Trade, Industry and Energy (MOTIE) and Korea Institute for Advancement of Technology (KIAT, Project No. P0011262).

## AUTHOR CONTRIBUTIONS

Y.K. designed this work and C.L. carried out all experiments, including device fabrication and measurements. H.K. involved in the analysis of spectroscopy data. C.L. and Y.K. wrote this manuscript.

## COMPETING INTERESTS

The authors declare no competing interests.

## ADDITIONAL INFORMATION

**Supplementary information** The online version contains supplementary material available at https://doi.org/10.1038/s41528-021-00105-z.

**Correspondence** and requests for materials should be addressed to Y.K.

**Reprints and permission information** is available at http://www.nature.com/reprints

**Publisher's note** Springer Nature remains neutral with regard to jurisdictional claims in published maps and institutional affiliations.